J Mater Sci: Mater Electron **(2025) 36:2092**

Study of charge transfer mechanisms in cobalt-substituted copper ferrites

Julia Mazurenko[1,2,*], Larysa Kaykan[1], Volodymyr Mokliak[1,3], Mateusz M. Marzec[4], Ludmila Matzui[2], Ludmila Vovchenko[2], and Olena Yakovenko[2]

[1] *Laboratory for Physics of Magnetic Films, G.V. Kurdyumov Institute for Metal Physics, N.A.S. of Ukraine, 36 Academician Vernadsky Boulevard, Kiev 03142, Ukraine*

[2] *Department of Physics, Taras Shevchenko National University of Kyiv, Volodymyrska 64/13, Kiev 01601, Ukraine*

[3] *Department of Physical and Mathematical Sciences, Ivano-Frankivsk National Technical University of Oil and Gas, Karpatska 15, Ivano-Frankivsk 76019, Ukraine*

[4] *Academic Centre for Materials and Nanotechnology, AGH University of Krakow, Av. Mickiewicza 30, 30-059 Krakow, Poland*

Received: 5 June 2025
Accepted: 9 November 2025
Published online: 18 November 2025

ABSTRACT

In this study, $Co_xCu_{1-x}Fe_2O_4$ (x = 0.0–1.0) spinel ferrites were synthesized by the citrate sol–gel autocombustion method and systematically investigated to clarify composition-dependent charge transport mechanisms. X-ray diffraction and FTIR confirmed spinel formation and revealed systematic cation redistribution with cobalt substitution. X-ray photoelectron spectroscopy (XPS) further verified the coexistence of Fe^{3+}/Fe^{2+} and Co^{2+}/Co^{3+} redox couples together with oxygen-vacancy–related states, providing direct evidence of multiple charge transfer pathways. Temperature-dependent conductivity showed thermally activated behavior, with a slope change above 373 K in Co-rich samples ($x \geq 0.8$), signaling a transition in the dominant conduction process. At low temperatures (298–348 K), transport was directed by grain boundary and defect-related hopping, while long-range small-polaron hopping between Fe^{2+}/Fe^{3+} dominated at elevated temperatures. Increasing Co content introduced additional Co^{2+}/Co^{3+} valence fluctuations, enhancing localized dielectric relaxation and structural disorder. AC conductivity analysis demonstrated decreasing activation energy with increasing frequency, consistent with enhanced carrier mobility. The data were successfully fitted using Jonscher's universal power law, its modified form, and the Almond–West model. Fitting revealed a composition-driven increase in onset frequency ω_H from ~ 4 kHz in $CuFe_2O_4$ to ~ 87 kHz in $CoFe_2O_4$, together with anomalously high dispersion parameters ($s > 1$, $m > 1$) in Co-rich samples, indicating strong interfacial polarization and dipolar relaxation. A distinct low-frequency break near 10 Hz in $CuFe_2O_4$ was attributed to structural transformation. The combined structural, spectroscopic, and electrical analyses demonstrating a clear evolution from long-range Fe^{2+}/Fe^{3+} hopping in Cu-rich ferrites to localized relaxation and interfacial polarization in Co-rich members. This tunability, linked to cation

Address correspondence to E-mail: yumazurenko@ifnmu.edu.ua

https://doi.org/10.1007/s10854-025-16193-w

distribution and oxygen-vacancy formation, positions $Co_xCu_{1-x}Fe_2O_4$ as a promising spinel system for high-frequency dielectric, EMI shielding, and microwave absorption applications.

1 Introduction

Magnetic nanoparticles, particularly spinel ferrites, have gained considerable attention due to their wide-ranging applications in biomedicine [1], catalysis [2], environmental remediation [3], ferrofluids [4], magnetic sensors [5], and high-frequency electronic devices [6]. Among these, spinel ferrites of the general formula MFe_2O_4 (where M is a divalent transition metal) are of particular interest because of their tunable electrical, magnetic, and dielectric properties, which can be tailored through synthesis conditions [7], particle size control, and ionic substitution strategies [8, 9].

The ability to manipulate these properties makes spinel ferrites attractive for use in a variety of technologies, including electromagnetic interference (EMI) shielding [10], microwave absorption [11], and energy storage [12]. With the rapid propagation of wireless communication systems, radar, and electronic devices, the issue of electromagnetic pollution has become a significant environmental and health concern. Prolonged exposure to high-frequency electromagnetic radiation has been linked to potential biological risks, prompting the urgent development of efficient electromagnetic wave absorbing materials [10, 11, 13–15].

Spinel ferrites have emerged as one of the most promising classes of magnetic materials for microwave absorption applications due to their inherent magnetic loss capability, high resistivity, and chemical stability. However, pure ferrites often suffer from limitations such as narrow absorption bandwidths, low attenuation efficiency, and poor impedance matching with free space, which restrict their practical utility [16–18]. To address these challenges, cation substitution – particularly with transition metal [19] or rare-earth ions [20] – has been widely adopted as a strategy to modulate the microstructure and enhance dielectric and magnetic properties. Such substitution can strongly influence key factors such as grain size, site occupancy, defect density, and conduction pathways, ultimately affecting the microwave absorption and charge transport characteristics of the material.

Among spinel ferrites, copper ferrite ($CuFe_2O_4$) is known for its mixed valence state of Fe and p-type conductivity [21]. However, its microwave and electrical performance can be significantly enhanced through partial substitution with cobalt [22, 23], which has a strong influence on the electronic structure and cation distribution. Cobalt ions (Co^{2+} and Co^{3+}) can occupy both tetrahedral (A) and octahedral (B) sites and participate in variable valence states, introducing new conduction channels and modifying relaxation dynamics. Despite extensive studies on ferrite systems, there remains a lack of detailed understanding of how cobalt substitution affects the conduction mechanisms of copper ferrite over wide temperature and frequency ranges, particularly when modeled using advanced dielectric fitting techniques.

The main objective of this work is to investigate the impact of cobalt substitution on the charge transport mechanisms in $Co_xCu_{1-x}Fe_2O_4$ (x = 0.0–1.0) ferrites synthesized via the citrate sol–gel autocombustion method. Special emphasis is placed on analyzing the temperature- and frequency-dependent conductivity, determining the activation energy of hopping processes, and identifying transitions in conduction behavior with increasing cobalt content. Unlike prior studies, this work applies a combination of Jonscher's universal power law, the modified Jonscher model, and the Almond–West model to extract detailed parameters such as dispersion exponents and onset frequency, offering multi-model understandings of dielectric relaxation and hopping dynamics.

By correlating electrical behavior with cation site distribution and microstructural changes, this study provides a deeper understanding of how cobalt ions alter polaron pathways and induce short-range relaxation effects. The novelty lies in the systematic multi-frequency, multi-model evaluation of conductivity in relation to composition, enabling the identification of a clear transition from long-range hopping to localized

dipolar relaxation in cobalt-rich ferrites. These insights are crucial for the rational design of spinel-based materials with optimized electromagnetic and electronic functionalities.

2 Synthesis and characterization techniques

2.1 Synthesis

Cobalt-substituted copper ferrite with the chemical composition $Co_xCu_{1-x}Fe_2O_4$ (where x = 0.0, 0.2, 0.4, 0.6, 0.8, and 1.0) was synthesized using the sol–gel autocombustion method [24]. Citric acid served as both the fuel and chelating agent, with a 1:1 molar ratio to the total metal ions, to promote the formation of a homogeneous precursor gel and facilitate spinel phase formation. In the synthesis process, stoichiometric amounts of cobalt nitrate [$Co(NO_3)_2{\cdot}6H_2O$], copper nitrate [$Cu(NO_3)_2{\cdot}3H_2O$], and ferric nitrate [$Fe(NO_3)_3{\cdot}9H_2O$] were used as precursors. All chemicals were procured from Loba Chemie, India, and were of analytical grade to ensure high purity and reproducibility. The pH of the precursor solution was adjusted to 7 using ammonia solution [25] and monitored with a digital pH meter to optimize the conditions for gel formation. The resulting mixture was continuously stirred and heated to promote gelation, followed by autocombustion, leading to the formation of ferrite powders. The obtained powders were subsequently ground and subjected to further studies.

It should be emphasized that the sol–gel autocombustion parameters strongly influence the resulting cation distribution. The chelating ratio and pH govern the stability of metal–citrate complexes, ensuring homogeneous mixing and controlled oxidation states before combustion. The fuel-to-nitrate balance dictates the intensity of the combustion front: rapid, highly exothermic combustion can freeze in non-equilibrium site occupancies, while slower combustion and post-combustion annealing promote redistribution toward thermodynamically stable configurations. These factors ultimately determine whether Cu^{2+} remains predominantly in B-sites or is displaced by Co^{2+}, and whether Co^{2+} migrates into both A- and B-sites. Since the electronic transport pathways in spinel ferrites rely on Fe^{3+}/Fe^{2+} and Co^{2+}/Co^{3+} redox couples, as well as oxygen vacancy concentration, the synthesis parameters provide a direct handle to tailor conduction and dielectric relaxation behavior in $Co_xCu_{1-x}Fe_2O_4$.

2.2 Characterization techniques

2.2.1 X-ray diffraction studies

Phase identification and structural analysis were performed on powdered samples using a Malvern Panalytical Empyrean diffractometer (UK) operating in Bragg–Brentano geometry with Cu Kα radiation (λ = 1.5406 Å). Instrumental broadening was corrected with a NIST LaB_6 standard. Diffraction data were analyzed by Rietveld refinement using the FullProf Suite software package, enabling determination of lattice parameters, crystallite size, and microstrain.

2.2.2 Fourier-transform infrared spectroscopy

Vibrational properties were investigated with a Bruker VERTEX 70v spectrometer (Germany) in the 400–4000 cm^{-1} spectral range at a resolution of 2 cm^{-1}. Samples were prepared as KBr pellets by thoroughly mixing the ferrite powders with spectroscopic-grade KBr and pressing the mixture into transparent discs. The acquired spectra were processed using OPUS software, with emphasis on peak assignment to tetrahedral and octahedral metal–oxygen vibrations.

2.2.3 X-ray photoelectron spectroscopy

Surface chemical states were probed using a PHI VersaProbeII Scanning XPS system equipped with a monochromatic Al Kα source (1486.6 eV). Measurements were acquired with a 100 μm beam spot at a 45° take-off angle. Survey spectra were collected at a pass energy of 117.5 eV, while high-resolution scans employed 46.95 eV. Charge compensation was achieved with dual-beam neutralization (7 eV Ar + ions and 1 eV electrons). All spectra were referenced to the C–C component of the C 1 s peak at 285.0 eV. The base pressure during analysis was below 3×10^{-7} mbar. Peak deconvolution was performed with PHI MultiPak software (v.9.9.3) using Shirley-type background subtraction.

2.2.4 Electrical and dielectric measurements

Ferrite powders were pressed into cylindrical pellets (10 mm diameter, 0.6 mm thickness) under a uniaxial pressure of 3 MPa and dried at 65 °C for 5 h. Graphite paste was applied to both flat surfaces to obtain a parallel-plate capacitor configuration. Dielectric and impedance measurements were performed using an Autolab PGSTAT100N impedance analyzer (Metrohm, Switzerland) in the frequency range 0.01 Hz–100 kHz. AC conductivity and the real (ε′) and imaginary (ε″) parts of the dielectric constant were evaluated. Temperature-dependent measurements were conducted up to 450 °C in 50 °C increments, with isothermal equilibration at each step to ensure thermal stability.

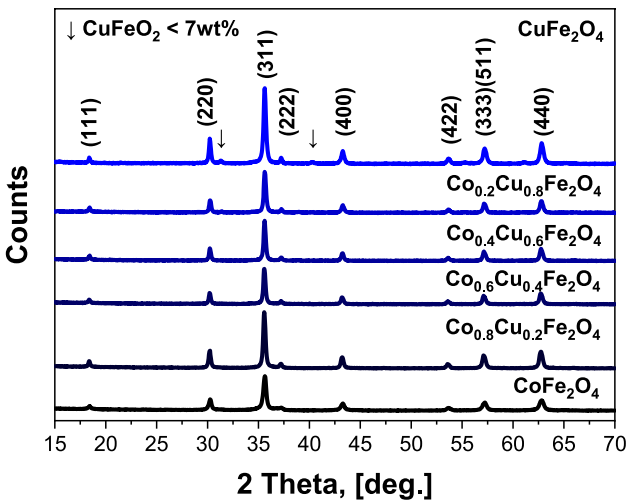

Fig. 1 X-ray diffraction patterns of $Co_xCu_{1-x}Fe_2O_4$ ($0.0 \le x \le 1.0$) prepared by the sol–gel autocombustion method [24]

3 Results and discussion

3.1 Structural and vibrational studies

Representative XRD patterns of $Co_xCu_{1-x}Fe_2O_4$ ($0.0 \le x \le 1.0$) are shown in Fig. 1. The unsubstituted sample (x = 0.0) contains mainly cubic spinel (Fd3m) with ~ 7 wt% $CuFeO_2$, which disappears upon cobalt incorporation, yielding phase-pure ferrites. A systematic shift of the (311) reflection with increasing Co content indicates lattice distortion due to the ionic radius difference between Cu^{2+} (0.73 Å) and Co^{2+} (0.74 Å). Williamson–Hall analysis (Table 1) shows a reduction in crystallite size (28 to 21 nm) and relaxation of lattice stress with cobalt substitution.

Cation distribution was determined from Rietveld refinement of the XRD patterns, where site occupancies of Cu^{2+}, Co^{2+}, and Fe^{3+} ions were refined under the constraints of stoichiometry (AB_2O_4), charge neutrality, and site multiplicities of the spinel structure. The relative scattering factors allowed estimation of how these cations redistribute between tetrahedral (A) and octahedral (B) sublattices with increasing cobalt substitution (Table 2). The results indicate that Co2 + ions progressively occupy both A- and B-sites, while Cu^{2+} remains preferentially octahedrally coordinated. This redistribution alters Fe–O–Co and Fe–O–Cu superexchange interactions and modifies Fe^{2+}/Fe^{3+} electron

Table 2 Cation distribution of $Co_xCu_{1-x}Fe_2O_4$ ferrites

Composition	Cation distribution
$CuFe_2O_4$	$(Cu_{0.36}Fe_{0.64})_A[Cu_{0.64}Fe_{1.36}]_B$
$Co_{0.2}Cu_{0.8}Fe_2O_4$	$(Co_{0.06}Cu_{0.48}Fe_{0.46})_A[Co_{0.14}Cu_{0.37}Fe_{1.54}]_B$
$Co_{0.4}Cu_{0.6}Fe_2O_4$	$(Co_{0.16}Cu_{0.28}Fe_{0.36})_A[Co_{0.24}Cu_{0.32}Fe_{1.64}]_B$
$Co_{0.6}Cu_{0.4}Fe_2O_4$	$(Co_{0.23}Cu_{0.17}Fe_{0.6})_A[Co_{0.37}Cu_{0.23}Fe_{1.4}]_B$
$Co_{0.8}Cu_{0.2}Fe_2O_4$	$(Co_{0.43}Cu_{0.16}Fe_{0.41})_A[Co_{0.37}Cu_{0.04}Fe_{1.59}]_B$
$CoFe_2O_4$	$(Co_{0.48}Fe_{0.52})_A[Co_{0.52}Fe_{1.48}]_B$

Table 1 Structural parameters of $Co_xCu_{1-x}Fe_2O_4$ ferrites

Co^{2+} content (x)	Lattice constant a (nm)	Cell volume (10^{-3} nm^3)	X-ray density (g/cm^3)	Crystallite size (nm)	Lattice stress
0.0	0.8368	586.140	5.422	28	0.00170
0.2	0.8381	588.672	5.218	24	0.00196
0.4	0.8383	588.236	5.218	23	0.00190
0.6	0.8384	589.340	5.218	22	0.00159
0.8	0.8383	589.199	5.218	24	0.00179
1.0	0.8379	588.302	5.217	21	0.00201

hopping, thereby influencing transport and photoactive properties. The XPS analysis presented in the following section provides independent evidence for these oxidation states and site preferences.

FTIR spectra [24] (Fig. 2) display the two characteristic spinel absorption bands: ~ 570–590 cm^{-1} (tetrahedral stretching) and ~ 400–430 cm^{-1} (octahedral vibrations). With increasing Co content, the octahedral band red-shifts from 413 cm^{-1} (x = 0.0) to 367 cm^{-1} (x = 1.0), while the tetrahedral band shifts only slightly (~ 4 cm^{-1}). A Cu–O feature near 650 cm^{-1}, evident in pure CuFe2O4, diminishes with cobalt substitution, consistent with Co2 + replacing Cu2 + in octahedral coordination.

X-ray diffraction, cation distribution, and FTIR confirm that cobalt incorporation stabilizes the spinel phase, introduces lattice distortion, and drives cation redistribution across A/B sites. These structural modifications are directly responsible for the observed changes in electronic transport and photoactivity, in line with earlier reports [24, 26, 27].

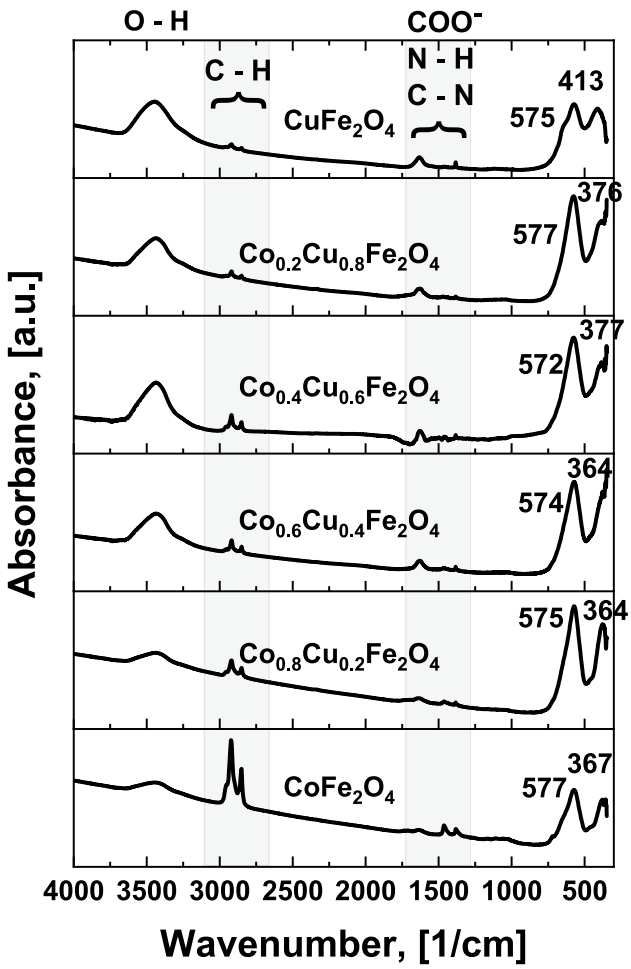

Fig. 2 Room-temperature FTIR spectra of $Co_xCu_{1-x}Fe_2O_4$ spinels: **a** 150–800 cm^{-1}. region highlighting metal–oxygen vibrations [24]

3.2 X-ray photoelectron spectroscopy analysis

To substantiate the cation distribution derived from refinement and to clarify the charge transfer mechanisms, XPS spectra of $Co_xCu_{1-x}Fe_2O_4$ (x = 0.0–1.0) were collected and deconvoluted (Fig. 3). The corresponding surface compositions are summarized in Table 3.

The Fe $2p_{3/2}$ spectra exhibit a main peak at ~ 710.2 eV accompanied by multiplet splitting and a shake-up satellite at ~ 718 eV, confirming Fe^{3+} as the predominant state [28, 29]. A minor Fe^{2+} component becomes more pronounced with cobalt substitution, supporting enhanced Fe^{3+}/Fe^{2+} electron hopping within the B-sublattice. This mechanism supports long-range small polaron conduction in Cu-rich ferrites and remains a key transport pathway even as cobalt is introduced.

The Cu 2p spectra display a component at 932.6 eV, attributable to Cu^0/Cu^+, together with strong shake-up satellites at ~ 943–945 eV that are diagnostic of Cu^{2+} [30, 31]. The Cu^{2+} contribution systematically decreases with increasing Co content, reflecting the progressive displacement of Cu from octahedral sites. Although the 932.6 eV feature may include contributions from both metallic Cu and Cu^+, the strong satellites confirm that Cu^{2+} remains dominant across the series. Quantitatively, the surface concentration of Cu^{2+} decreases from ~ 4.1 at.% for x = 0.0 to only ~ 0.6 at.% for x = 1.0, while the Co signal rises from 0 to ~ 11.6 at.% (Table 3). This trend is consistent with the redistribution of cations obtained from XRD refinement and illustrates the gradual replacement of the Fe–O–Cu superexchange network by Fe–O–Co interactions.

Co analysis was carried out using the Co 3 s region, given the overlap of Co 2p with Fe Auger features. A main peak at ~ 101.7 eV with a characteristic multiplet splitting of ~ 5.5 eV confirms high-spin Co^{2+}, while a weaker higher-energy shoulder indicates partial oxidation to Co^{3+} in Co-rich ferrites (x ≥ 0.6) [32, 33]. The coexistence of Co^{2+} and Co^{3+} has important implications: in addition to Fe^{3+}/Fe^{2+} hopping, valence fluctuations of Co^{2+}/Co^{3+} introduce new localized conduction pathways, particularly at higher cobalt content. These additional redox-active centers favor short-range relaxation processes, which explains the anomalous dielectric dispersion and localized polarization

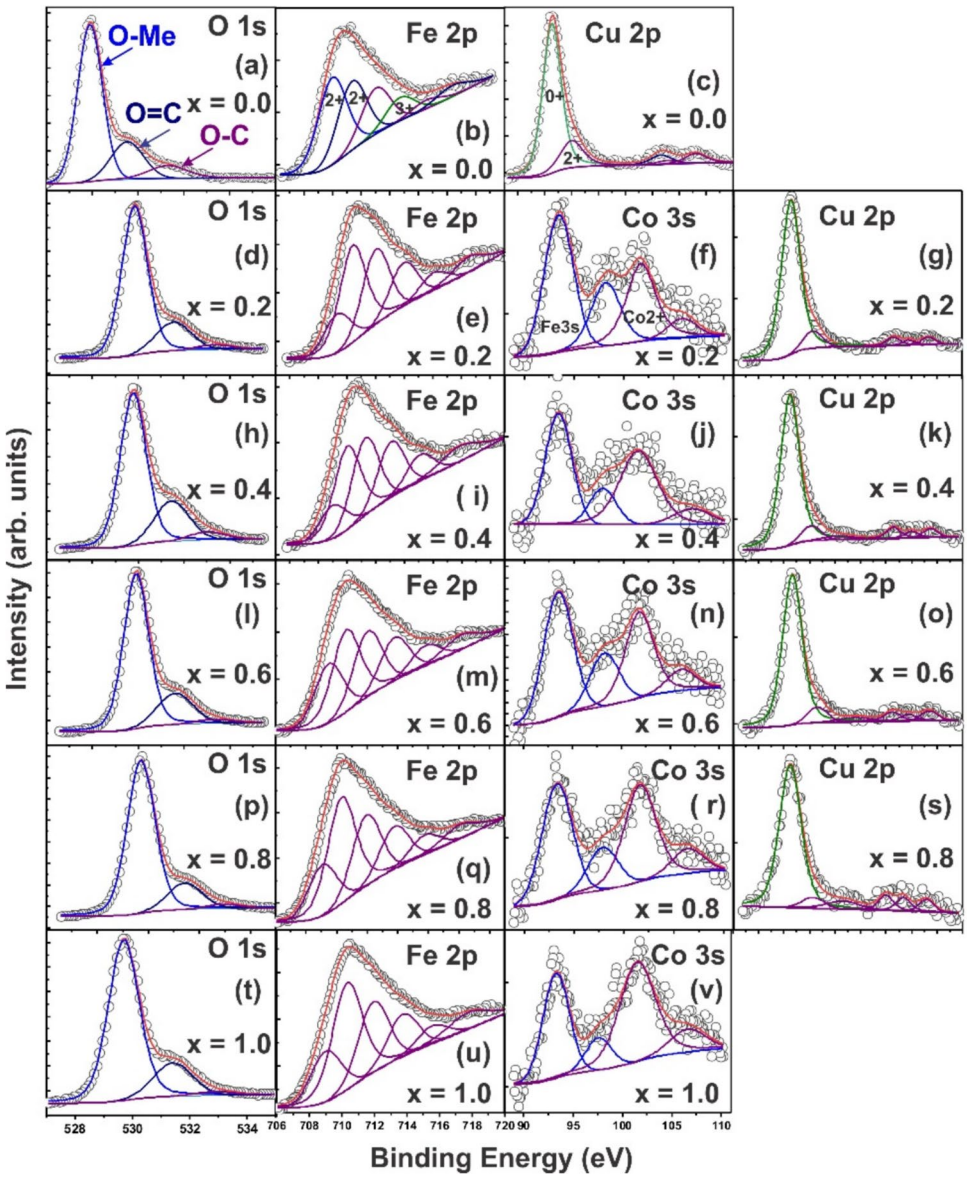

Fig. 3 High-resolution XPS spectra of $Co_xCu_{1-x}Fe_2O_4$ spinels. Panels show deconvoluted O 1 s, Fe 2p, Cu 2p, and Co 3 s regions, indicating the coexistence of Cu^{2+}, Fe^{3+}/Fe^{2+}, and Co^{2+}/Co^{3+} oxidation states together with lattice oxygen and surface defect contributions

Table 3 Surface composition (atomic %) determined by fitting XPS spectra for all analyzed samples

	C			N	O			Fe	Co	Cu	
Energy [eV]	285.0	286.5	288.6	398.8	529.8	531.5	533.1	709.2	101.7	932.6	934.6
Sample	C–C	C–O–C	O-C = O	C-N = C	O-Fe O-Co O-Cu	O = C	O-C, OH	Fe^{3+}	Co^{2+}	Cu^0	Cu^{2+}
$CuFe_2O_4$	19.1	3.6	3.4	–	33.4	10.1	4.7	15.3	–	6.3	4.1
$Co_{0.2}Cu_{0.8}Fe_2O_4$	12.3	2.4	4.1	1.3	42.4	10.1	1.6	10.7	2.5	10.5	2.1
$Co_{0.4}Cu_{0.6}Fe_2O_4$	12.9	4.1	5.1	1.8	39.2	12.4	2.5	9.8	2.7	7.7	1.9
$Co_{0.6}Cu_{0.4}Fe_2O_4$	12.8	2.1	4.0	0.9	43.6	11.2	1.4	11.3	3.1	7.6	2.1
$Co_{0.8}Cu_{0.2}Fe_2O_4$	12.2	0.8	3.4	0.8	49.2	9.8	1.6	13.3	4.2	3.7	1.3
$CoFe_2O_4$	13.2	1.1	3.4	0.5	49.3	11.6	1.2	14.4	4.7	0.0	0.6

observed in the frequency-dependent conductivity of Co-rich samples.

The O 1 s spectra can be resolved into three components: lattice oxygen in metal–oxygen bonds (~ 529.8 eV), defective oxygen or oxygen bound to carbon (~ 531.5 eV), and hydroxyl/adsorbed species (~ 533.1 eV). The defective oxygen fraction increases from ~ 10.1 at.% (x = 0.0) to ~ 11.6 at.% (x = 1.0), indicating enhanced lattice disorder and oxygen vacancy formation with cobalt substitution. Such non-stoichiometric oxygen plays a dual role: it facilitates charge compensation during cation redistribution and provides additional localized states for carrier trapping, further enhancing dielectric relaxation and interfacial polarization effects.

The XPS analysis establishes that Fe remains predominantly Fe^{3+} with minor Fe^{2+}, Cu is mainly Cu^{2+} with traces of Cu^{0}/Cu^{+}, and Co is largely Co^{2+} with partial Co^{3+} in highly substituted ferrites. The simultaneous presence of Fe^{3+}/Fe^{2+} and Co^{2+}/Co^{3+} redox couples, coupled with an increased concentration of oxygen defects, generates multiple charge-transfer channels. This spectroscopic evidence directly supports the composition-driven transition identified in the transport and dielectric studies: from long-range polaron hopping dominated by Fe^{3+}/Fe^{2+} in Cu-rich ferrites to localized relaxation and interfacial polarization mechanisms governed by Co redox chemistry and oxygen-vacancy-assisted conduction in Co-rich compositions.

3.3 Analysis of electrical transport properties

The electrical transport properties were explored through temperature-dependent AC and DC conductivity measurements. Figure 4 shows the variation of ln(σT) with 1000/T for DC conductivity, demonstrating a thermally activated conduction mechanism across all compositions.

Notably, for samples with high cobalt substitution levels (x = 0.8 and 1.0), a distinct inflection point in the high-temperature regime (T ≥ 373 K) suggests a change in the dominant conduction mechanism. Such behavior is often indicative of a transition from small polaron hopping at low temperatures to variable-range hopping or mixed-valence conduction at elevated temperatures [34]; however, as later discussed in the context of Jonscher and Almond–West model fittings, these changes may instead reflect a shift toward localized dielectric relaxation and interfacial polarization in Co-rich compositions.

The temperature dependence of electrical conductivity, interpreted within the framework of hopping conduction theory, is described by the following expression [35]:

$$\sigma = \frac{ne^2d^2\nu}{kT}\exp\left(\frac{-W_H}{kT}\right) \quad (1)$$

Here e represents the elementary charge of an electron, n denotes the concentration of charge carriers, and d is the hopping length of charge carriers, corresponding to the average distance between adjacent octahedral sites (~ 0.295 nm) in the investigated compounds. Value k refers to the Boltzmann constant, while ν is the threshold activation frequency associated with the hopping process. The value of ν was estimated from the IR spectra [24] (Table 4). Finally, W_H represents the hopping activation energy.

The activation energies derived from the linear regions of ln(σT) vs. 1000/T plots confirm that hopping conduction is dominant at low to moderate temperatures.

Figure 2 presents the temperature dependence of AC conductivity for all samples across a range of measurement frequencies. (Figure 5)

At lower temperatures (298–348 K), the AC conductivity exhibits weak temperature dependence but strong frequency sensitivity, consistent with Maxwell–Wagner interfacial polarization [36] and hopping conduction through localized states [37]. These localized states likely originate from structural inhomogeneities, oxygen vacancies, and interfacial grain boundaries [38]. The change in slope at higher temperatures suggests enhanced thermally activated mobility of carriers [39], which may be influenced by the emergence of interfacial polarization effects and Co^{3+}/Co^{2+} redox dynamics. These mechanisms become more pronounced in Co-rich compositions and are consistent with the localized relaxation behavior observed in the dielectric analysis and possibly a change in the dominant charge transfer path. For cobalt-rich compositions, such behavior could be related to the increased presence of Co^{3+}/Co^{2+} redox pairs and altered cation distribution in the spinel lattice, modifying both hopping distances and available conduction pathways.

In the temperature range of 348–448 K, electrical conductivity exhibits a pronounced increase with rising temperature. In this regime, the carrier

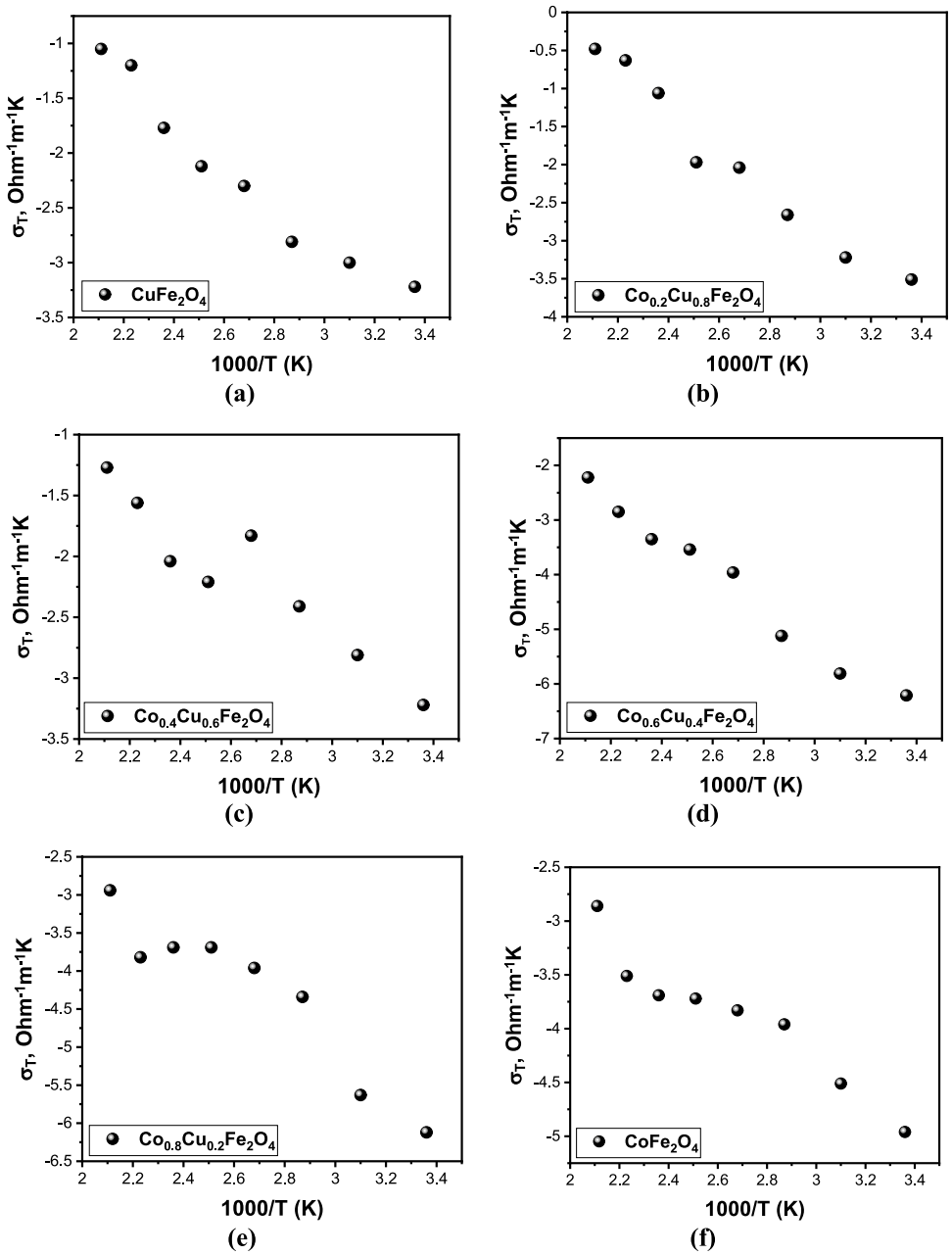

Fig. 4 Temperature dependence of DC conductivity for $Co_xCu_{1-x}Fe_2O_4$ systems

Table 4 IR absorption band of the B-site and the corresponding threshold activation frequency (ν) estimated from IR spectra

Sample	IR absorption band of the B-site, cm^{-1}	Threshold activation frequency, $\nu \times 10^{13}$, Hz
$CuFe_2O_4$	413	1.768
$Co_{0.2}Cu_{0.8}Fe_2O_4$	376	1.610
$Co_{0.4}Cu_{0.6}Fe_2O_4$	377	1.614
$Co_{0.6}Cu_{0.4}Fe_2O_4$	364	1.559
$Co_{0.8}Cu_{0.2}Fe_2O_4$	364	1.557
$CoFe_2O_4$	367	1.572

concentration remains nearly constant, as the thermal energy is insufficient to excite electrons across the band gap into extended conduction states [40]. Instead, the observed enhancement in conductivity is attributed to increased mobility of localized charge carriers, consistent with small polaron hopping rather than band conduction. This conclusion is further supported by the behavior of the Jonscher exponent s and Almond–West dispersion parameter n, both of which indicate thermally activated hopping in this temperature range for Cu-rich compositions.

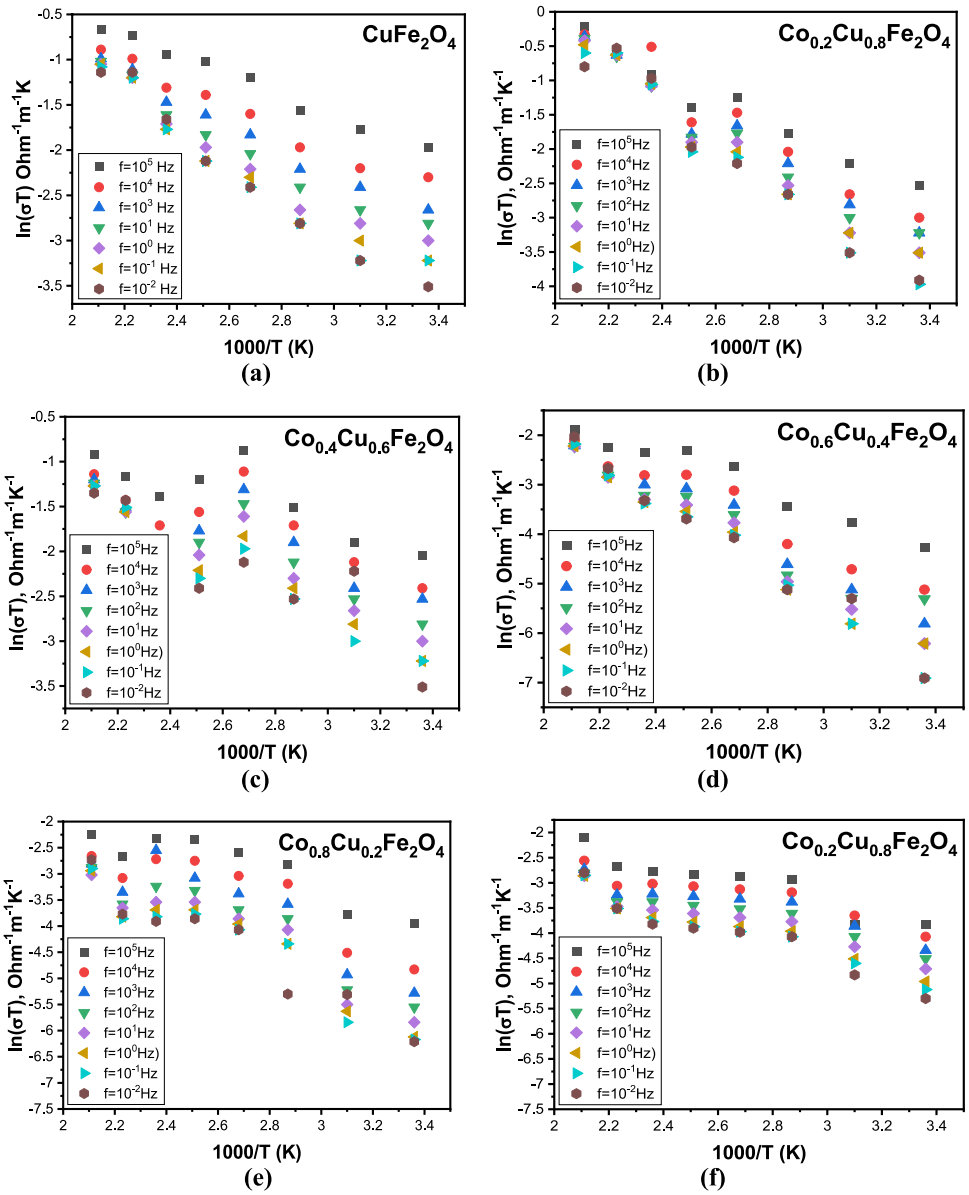

Fig. 5 Temperature dependence of AC conductivity for samples with composition $Co_xCu_{1-x}Fe_2O_4$ at different frequencies

In ferrites, charge carriers are localized on transition metal ions [41], and conductivity primarily originates from electron exchange between ions in different valence states. In particular, electron hopping between Fe^{3+}/Fe^{2+} and Co^{3+}/Co^{2+} pairs play a key role. Due to their larger ionic radius, Fe^{2+} ions preferentially occupy the octahedral (B) sites, making them the principal contributors to the hopping mechanism in the studied spinel structure.

In the dispersive region (Region II), the activation energy (E_a) for conductivity decreases with increasing frequency (Fig. 3), indicative of a hopping conduction mechanism. At higher frequencies, the energy barrier for carrier transitions between localized states is reduced, aligning with the predictions of small polaron hopping theory.

Charge transport in semiconducting ferrites is typically governed by two primary mechanisms [34]: hopping conduction and band-like (activation) conduction. These are distinguished by the density of localized states near the Fermi level and the available thermal energy [42, 43]: hopping conduction dominates when the density of localized states is high. In this regime, charge carriers move between neighboring localized states via phonon-assisted hopping, without excitation into extended bands. This process is prominent

at lower temperatures and/or high frequencies, where short-range mobility governs charge transport; band conduction (activation mechanism) becomes significant at elevated temperatures when thermal energy is sufficient to excite carriers into the conduction or valence bands. In this case, carriers move as extended states under an external electric field, and conductivity follows the Arrhenius law.

Both mechanisms can coexist, with a crossover in dominance observable through changes in the temperature dependence of conductivity. Specifically, a linear relationship in a $\ln(\sigma T^{-1})$ vs. 1/T plot indicates thermally activated transport governed by the Arrhenius equation [44]:

$$\sigma(E) = \sigma_0 \exp\left(-\frac{\Delta E}{kT}\right) \tag{2}$$

where ΔE is the activation energy for the conduction process (measured in eV); k denotes the Boltzmann constant, and σ_0 is the pre-exponential factor, representing the conductivity at T = 0 K (an approximate value).

This expression describes the thermally activated transport of charge carriers, where electrical conductivity increases with temperature as carriers acquire sufficient energy to overcome potential barriers between localized states or within energy bands. The slope of the linear plot in $\ln(\sigma T^{-1})$ coordinates allows direct determination of the activation energy (ΔE), providing insight into the dominant conduction mechanism in the investigated material.

To determine the activation energy, data points are selected at the boundaries of the linear region in the temperature dependence of electrical conductivity. From these points, perpendicular lines (normals) are projected onto the coordinate axes, yielding the values σ_1, σ_2, T_1, and T_2 [45]:

$$\ln \sigma_1 = \ln \sigma_0 - \frac{\Delta E}{kT_1} \tag{3}$$

$$\ln \sigma_2 = \ln \sigma_0 - \frac{\Delta E}{kT_2} \tag{4}$$

By subtracting the logarithmic form of the conductivity equation term by term, the following relationship is derived:

$$\ln \sigma_1 - \ln \sigma_2 = \frac{\Delta E}{k}\left(\frac{1}{T_2} - \frac{1}{T_1}\right) \tag{5}$$

From this expression, the activation energy can be calculated as [45]:

$$\Delta E = \frac{\ln \frac{\sigma_1}{\sigma_2} T_1 T_2}{k(T_1 - T_2)} \tag{6}$$

As shown in Fig. 3, activation energy decreases with increasing frequency, further confirming the hopping nature of conduction. This frequency dependence of E_a reflects the reduced thermal energy required for charge carrier transitions at higher frequencies and supports the interpretation based on localized polaronic transport. (Figure 6)

The activation energy associated with hopping conduction in $Co_xCu_{1-x}Fe_2O_4$ ferrites decreases notably with increasing frequency. Its behavior is well-explained by Koops' phenomenological model [46], which treats ferrites as inhomogeneous dielectric materials composed of well-conducting grains (crystallites) separated by poorly conducting grain boundaries. These grain boundaries typically harbor a high density of structural defects that serve as charge carrier traps, impeding electron mobility, particularly at low frequencies.

At lower frequencies, charge transport is dominated by the grain boundaries and interphase regions, where defects lead to higher activation energies and lower conductivities. As the measurement frequency

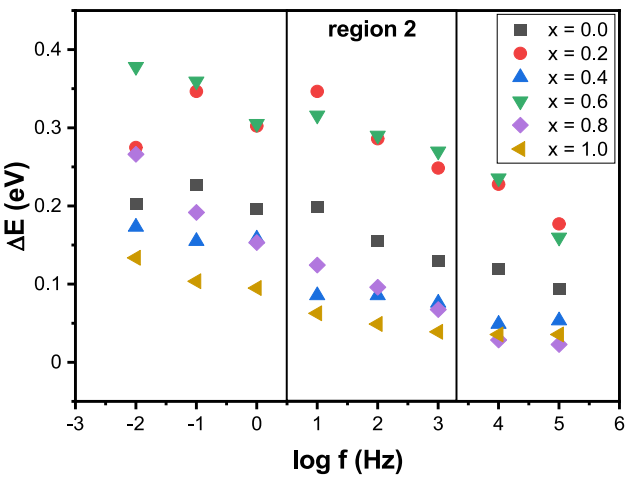

Fig. 6 Variation of the activation energy (Ea) for hopping conductivity as a function of frequency for $Co_xCu_{1-x}Fe_2O_4$ ferrites. Ea decreases systematically with increasing frequency, confirming thermally activated small polaron hopping. The strongest frequency dependence is observed in Cu-rich samples, while Co-rich compositions show reduced Ea values, consistent with the emergence of localized relaxation pathways

increases, the applied alternating field enhances the probability of localized electron hopping between transition metal ions of variable valence, such as Fe^{3+}/Fe^{2+} and Co^{3+}/Co^{2+}. Under high-frequency excitation, polarization of the electron clouds occurs more rapidly, thereby facilitating valence fluctuation and short-range charge transfer [47]. This dynamic reduces the effective energy barrier, resulting in lower activation energies and enhanced conductivity at elevated frequencies [48].

The dominant hopping mechanism also evolves with increasing cobalt substitution. At low cobalt ion concentrations, the primary contribution to the hopping conduction mechanism arises from the valence transition $Fe^{3+} + e^{-} \rightarrow Fe^{2+}$, which predominantly occurs at the B-sites of the spinel structure due to the octahedral coordination preference of Fe^{2+}. However, as the cobalt content increases, cobalt ions begin to actively participate in the conduction process.

The smaller ionic radius of Co^{3+} compared to Co^{2+}, along with the ability of Co^{2+} to occupy both A-sites (tetrahedral) and B-sites (octahedral), introduces an additional conduction pathway: $Co^{2+} + h^{+} \leftrightarrow Co^{3+}$. This redox mechanism can occur within both sublattices, further enhancing the electrical conductivity of the material.

Therefore, the overall conductivity in these ferrites is governed not only by the cobalt content, but also by the specific cation distribution across A and B sites in the spinel lattice. The refined cation distribution, derived via cationic occupancy modeling and previously reported in [24], is presented in Table 2.

Figure 4 presents the dependence of the B-site Fe ion concentration and the corresponding activation energy for hopping conduction on cobalt content. (Figure 7)

The results show an inverse correlation between the Fe concentration at B-sites and the hopping activation energy. As the number of Fe ions participating in Fe^{3+}/Fe^{2+} hopping decreases due to substitution by Co, the contribution of Co-mediated conduction increases. This compositional transition is reflected in the non-linear behavior of $\ln(\sigma_T)$ vs. 1000/T plots at high cobalt levels, indicating a dual-conduction mechanism involving both Fe^{3+}/Fe^{2+} and Co^{3+}/Co^{2+}redox pairs.

3.4 Analysis of dielectric properties with theoretical correlation

In spinel ferrites, dielectric behavior is governed by the interplay of cation distribution, structural disorder, grain boundary effects, and thermally activated charge dynamics [49, 50]. These factors influence both carrier mobility and the polarization response under an external field. To disentangle these contributions, three theoretical models were employed in a complementary fashion. Jonscher's universal power law was first applied to describe frequency-dependent conductivity in Cu-rich samples, where long-range polaron hopping between Fe^{2+}/Fe^{3+} dominates and the exponent s remains within its physical range ($0 < s < 1$). However, in Co-rich ferrites, anomalous values ($s > 1$) revealed that a single-exponent description was insufficient. In these cases, the modified Jonscher model was used, introducing two exponents (n and m) to separately capture low-frequency hopping processes and high-frequency localized relaxation. Finally, the Almond–West model was employed to quantify the dynamic crossover between DC and AC conduction via the onset frequency ω_H, which provides a direct measure of carrier hopping rates. Together, these models establish a coherent framework: Jonscher identifies

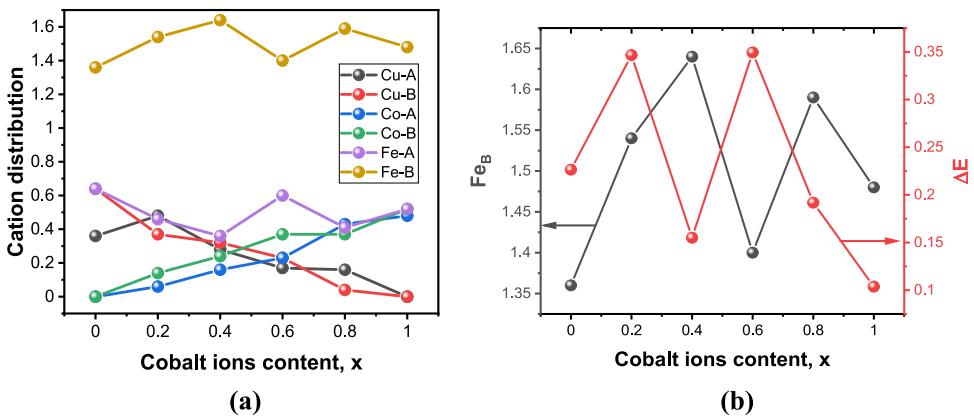

Fig. 7 Dependence of the iron ion concentration in the B-sublattice and the activation energy for hopping conduction on the cobalt ion content in $Co_xCu_{1-x}Fe_2O_4$ ferrites

the dominant conduction mechanism, the modified Jonscher resolves coexisting hopping and relaxation processes, and Almond–West quantifies their frequency-domain dynamics across the $Co_xCu_{1-x}Fe_2O_4$ series.

3.4.1 Joncher's power law fit

Jonscher's universal power law is widely applied to disordered systems, particularly ferrites, where conduction occurs via thermally activated hopping between localized states. It describes the frequency dependence of the real part of AC conductivity as [51]:

$$\sigma(\omega) = \sigma_{DC} + A\omega^s \quad (7)$$

Here σ_{DC} is the frequency – independent DC conductivity; A is a temperature – dependent constant; $\omega = 2\pi f$ is the angular frequency; s is the frequency exponent, typically $0 < s < 1$.

The value of the power s reflects the dominant conduction mechanism. Values near 1 suggest long-range translational motion or ideal Debye-type behavior, whereas lower values ($s < 1$) indicate short-range hopping conduction, typical of ferrites with localized charge transport via Fe^{2+}/Fe^{3+} transitions at B-sites.

The frequency-dependent AC conductivity data at room temperature for $Co_xCu_{1-x}Fe_2O_4$ ferrites, presented in Fig. 5, exhibit a typical dispersive behavior that is well-described by Jonscher's Power Law, as evidenced by the close agreement between the experimental data and the fitted curves. (Figure 8)

For Cu-rich compositions ($x = 0.0–0.4$), the values range from 0.558 to 0.682 (Table 5), which is consistent with long-range polaron hopping via Fe^{2+}/Fe^{3+} pairs in a moderately disordered spinel lattice. In this regime, Cu^{2+} ions occupy octahedral sites without significantly disrupting the Fe^{2+}/Fe^{3+} hopping network.

In contrast, Co-rich compositions ($x \geq 0.6$) exhibit high s values (1.180–1.351), which exceed the theoretical limits of the classical model. Such values imply an unphysical super-linear increase in conductivity with frequency and indicate that a single hopping mechanism is no longer sufficient to describe the dielectric response. This behavior is attributed to the increased substitution of Co^{2+} ions, which alters the cation distribution, introduces stronger structural distortion, and enhances localization of carriers. The redistribution of Co^{2+} into both tetrahedral and octahedral sites disrupts the Fe^{2+}/Fe^{3+} network and promotes the emergence of interfacial polarization and short-range relaxation processes [52], particularly at high frequencies. An alternative explanation for the observed increase in the power-law exponent may be the contribution of additional conduction processes to the overall transport mechanism [53]. Specifically, increasing cobalt concentration introduces a higher density of charge carriers, thereby enhancing conductivity through supplementary pathways such as Co2 + /Co3 + valence fluctuations.

3.4.2 Temperature-dependent evolution of the Jonscher exponent

To better understand the conduction dynamics in $Co_xCu_{1-x}Fe_2O_4$ ferrites, the variation of the Jonscher frequency exponent s was analyzed as a function of temperature from 300 to 475 K (Table 6, Fig. 9). The exponent s offers insight into the underlying conduction mechanism: values.

$s < 1$ typically reflect hopping conduction (as described by the CBH model [54]), whereas $s > 1$ suggests more complex behaviors, including interfacial polarization or fit artifacts when a single power law becomes insufficient.

As seen in Fig. 8, Cu-rich samples ($x = 0.0, 0.2, 0.4$) exhibit an overall decrease in s with increasing temperature, especially notable for $x = 0.4$ (from 0.524 at 300 K to 0.271 at 375 K). This trend supports the Correlated Barrier Hopping (CBH) mechanism [54], where higher temperatures enhance carrier mobility and reduce the frequency dispersion of AC conductivity. It also aligns with the small polaron hopping model, in which thermally activated electrons hop between localized Fe^{2+}/Fe^{3+} states at octahedral sites. A partial recovery of s at higher temperatures (e.g., 0.844 at 475 K for $x = 0.4$) could reflect thermal activation of additional hopping pathways or onset of interfacial effects.

In contrast, Co-rich compositions ($x = 0.6, 0.8, 1.0$) start with anomalously high s values at 300 K (1.46–1.35), exceeding the theoretical range of Jonscher's model. These values suggest dominance of localized dielectric relaxation, possibly linked to interfacial polarization or grain boundary effects. For $x = 0.6$, s gradually decreases with temperature, consistent with a transition toward thermally assisted hopping. However, for $x = 1.0$ ($CoFe_2O_4$), the exponent remains close to or above unity across the temperature

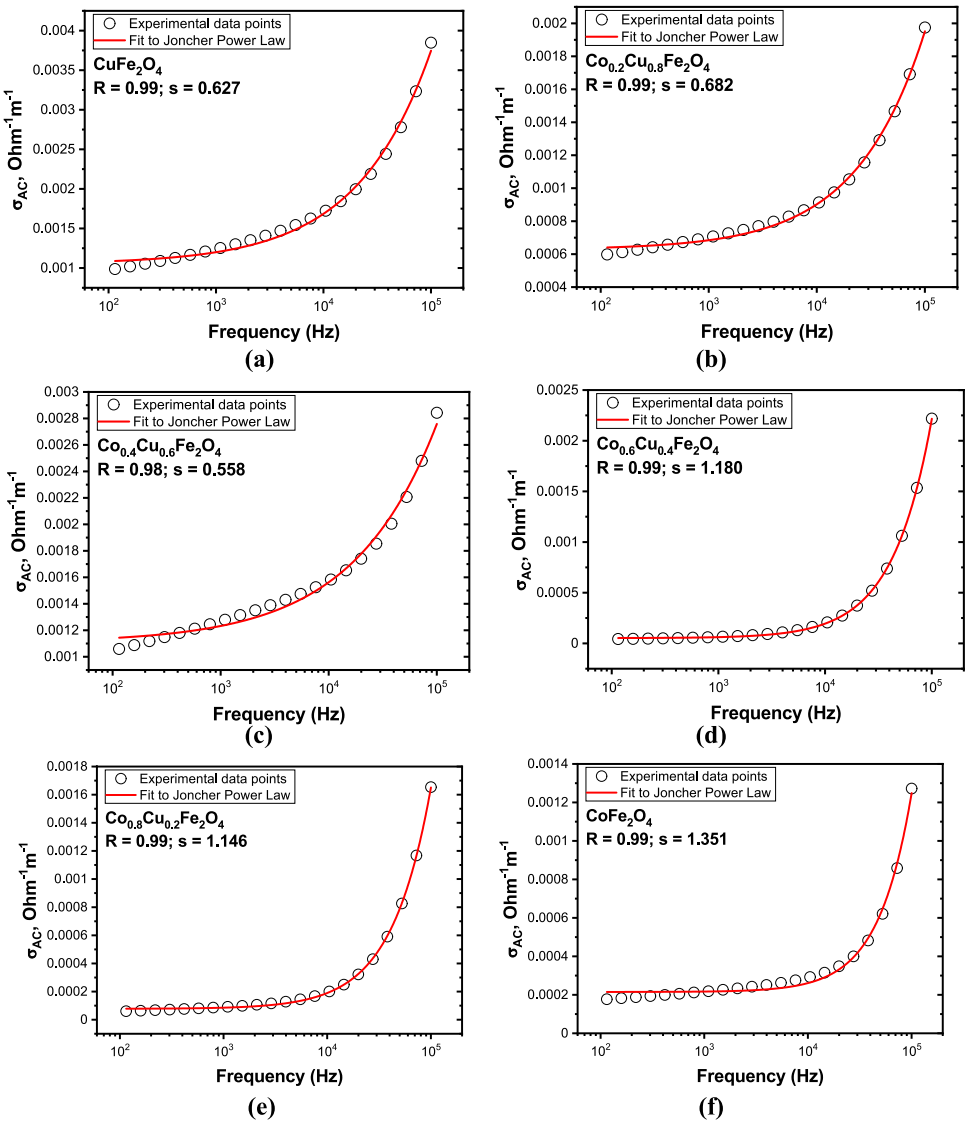

Fig. 8 Frequency dependence of AC conductivity for $Co_xCu_{1-x}Fe_2O_4$ ferrites at room temperature, with solid lines representing fits to Jonscher's Power Law model. Cu-rich samples ($x \leq 0.4$) display typical sublinear dispersion ($s < 1$), characteristic of long-range hopping conduction, while Co-rich samples ($x \geq 0.6$) exhibit anomalously steep slopes ($s > 1$), indicating a transition toward dipolar relaxation and interfacial polarization effects

Table 5 Summarizes the fitted Jonscher's and modified Jonscher's exponents for $Co_xCu_{1-x}Fe_2O_4$ ferrites

Composition	Jonscher s	R^2	Modified Jonscher n	Modified Jonscher m	R^2
$CuFe_2O_4$	0.627	0.99	–	–	–
$Co_{0.2}Cu_{0.8}Fe_2O_4$	0.682	0.99	–	–	–
$Co_{0.4}Cu_{0.6}Fe_2O_4$	0.558	0.98	–	–	–
$Co_{0.6}Cu_{0.4}Fe_2O_4$	1.180	0.99	0.142	1.217	0.99
$Co_{0.8}Cu_{0.2}Fe_2O_4$	1.146	0.99	0.153	1.227	0.99
$CoFe_2O_4$	1.351	0.99	0.146	1.770	0.99

range, indicating persistent short-range relaxation or composite-like dielectric behavior.

Notably, at 425 K, a discontinuous jump in s is observed for several compositions: for $x = 0.2$, s increases from 0.682 to 0.929; for $x = 0.4$, from 0.558 to 0.665. This discontinuity may result from a microstructural transition, such as cation redistribution between tetrahedral and octahedral sites or thermally induced strain near grain boundaries, temporarily increasing carrier localization and enhancing frequency dispersion [55].

These temperature trends provide strong evidence for a compositionally tunable conduction mechanism: for Cu-rich samples favor long-range hopping at elevated temperatures, for Co-rich samples exhibit

Table 6 Jonscher exponent s versus temperature for $Co_xCu_{1-x}Fe_2O_4$ ferrites (x = 0.0–1.0), showing the evolution of conduction mechanisms with composition and temperature

Temperature, K	Jonscher exponent s					
	x = 0.0	x = 0.2	x = 0.4	x = 0.6	x = 0.8	x = 1.0
300	0.627	0.682	0.558	1.180	1.146	1.351
325	0.568	0.605	0.398	0.984	0.932	1.057
350	0.523	0.476	0.350	0.910	0.452	0.892
375	0.552	0.394	0.271	0.870	0.627	0.792
400	0.526	0.365	0.482	0.851	0.550	0.692
425	0.590	0.929	0.665	0.931	0.627	1.227
450	0.656	0.896	0.768	1.006	0.939	1.148
475	0.776	0.654	0.844	1.175	0.990	1.014

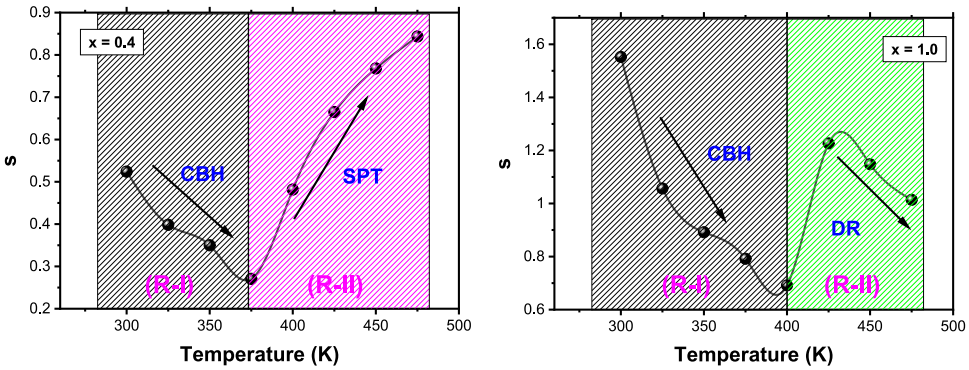

Fig. 9 Temperature dependence of the Jonscher exponent s for Co0.4Cu0.6Fe2O4 (x = 0.4) and CoFe2O4 (x = 1.0). For x = 0.4, two distinct conduction regions are observed: (R-I) a decreasing s trend with temperature from 300 to 375 K, characteristic of small polaron hopping (CBH model), and (R-II) an increasing s trend above 375 K, suggesting the onset of localized dielectric relaxation. In contrast, the Co-rich sample (x = 1.0) exhibits s > 1 over most of the range, indicating dominant dipolar relaxation and interfacial polarization mechanisms

localized relaxation mechanisms, likely associated with enhanced disorder and cation substitution.

3.4.3 *Modified Joncher's power law fit*

To describe the frequency response of Co-rich samples, the modified Jonscher power law was applied [56]:

$$\sigma(\omega) = \sigma_{DC} + A\omega^n + B\omega^m \quad (8)$$

where the exponents n and m capture low-and high-frequency dispersion, respectively (Fig. 9).

As summarized in Table 5, the low-frequency exponent n (0.142–0.153) indicates that hopping conduction remains active, though increasingly constrained as cobalt content rises. In contrast, the high-frequency exponent m grows markedly with substitution—from 1.217 for Co0.6Cu0.4Fe2O4 to 1.770 for CoFe2O4 – signaling a stronger contribution from dipolar relaxation and interfacial polarization at elevated cobalt levels [57, 58]. (Figure 10)

These results demonstrate that cobalt incorporation progressively suppresses extended polaron pathways and enhances localized dielectric processes, producing a mixed conduction regime where both hopping and relaxation mechanisms coexist.

3.4.4 *Almond–west model analysis*

To complement the Jonscher analysis and obtain dynamic parameters of carrier relaxation, the Almond–West model was applied to the AC conductivity data. Unlike Jonscher's framework, which characterizes dispersion behavior, the Almond–West model introduces the onset frequency

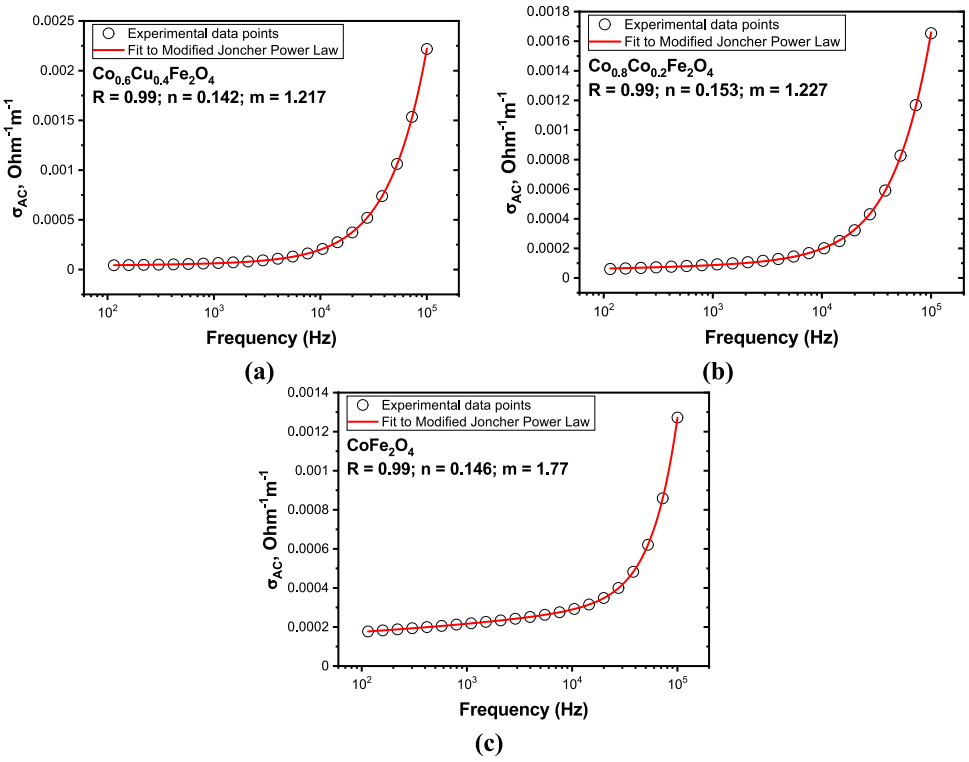

Fig. 10 Modified Jonscher power law model applied to Co-rich $Co_xCu_{1-x}Fe_2O_4$ ferrites, capturing both long-range hopping (n) and localized relaxation (m) effects

Table 7 Almond–West model fitting for $Co_xCu_{1-x}Fe_2O_4$ ferrites

Composition	n	ω_H, Hz	R^2
$CuFe_2O_4$	0.38	14,524.9	0.97
$Co_{0.2}Cu_{0.8}Fe_2O_4$	0.39	32,037.5	0.96
$Co_{0.4}Cu_{0.6}Fe_2O_4$	0.23	4239.8	0.97
$Co_{0.6}Cu_{0.4}Fe_2O_4$	1.14	17,808.5	0.99
$Co_{0.8}Cu_{0.2}Fe_2O_4$	1.07	25,483.8	0.99
$CoFe_2O_4$	1.00	87,029.4	0.95

(ω_H), corresponding to the average hopping or relaxation rate of mobile charge carriers [56, 59]:

$$\sigma(\omega) = \sigma_{DC}\left[1 + \left(\frac{\omega}{\omega_H}\right)^n\right] \quad (9)$$

where ω_H defines the frequency at which conductivity transition from frequency independent (DC) to frequency dependent (AC) behavior, and the exponent n reflects the degree of dispersion related to hopping dynamics.

The fitting results (Table 7) reveal a clear compositional dependence. In Cu-rich ferrites ($x \le 0.4$), n lies well below unity (0.234–0.392), and ω_H remains relatively low (4–32 kHz). These values are consistent with long-range Fe2 + /Fe3 + polaron hopping across continuous B–O–B pathways, where carriers require higher thermal activation to participate in conduction.

As cobalt content increases ($x \ge 0.6$), ω_H rises sharply, reaching nearly 87 kHz in $CoFe_2O_4$, while n approaches or slightly exceeds unity (1.0–1.15). This reflects faster carrier dynamics dominated by short-range relaxation and interfacial processes. The steep increase in ω_H indicates that localized hopping and dipolar polarization processes occur at much shorter timescales than in Cu-rich ferrites. Such behavior is consistent with enhanced structural disorder, oxygen vacancy formation, and cation redistribution, which fragment the Fe–O–Fe hopping network and favor Co^{2+}/Co^{3+} valence fluctuations. In addition, Maxwell–Wagner-type interfacial polarization at grain boundaries likely contributes to the relaxation features observed in Co-rich samples, reinforcing the role of microstructural heterogeneity.

Taken together, the Almond–West parameters demonstrate a composition-driven transition from slow, long-range hopping conduction in Cu-rich samples to fast, localized dielectric relaxation in Co-rich ferrites. Importantly, ω_H serves as a quantitative marker of this transition, providing direct evidence that Co substitution accelerates carrier dynamics and increases the frequency window where relaxation dominates.

These insights highlight the importance of using complementary models: while the modified Jonscher approach identifies the coexistence of hopping and relaxation processes, the Almond–West analysis quantifies their dynamic crossover through ω_H. This dual-model perspective reinforces the strong coupling between cation distribution, oxygen vacancy concentration, and charge carrier mobility in mixed-metal ferrite systems.

Due to their tunable conduction mechanisms, enhanced dielectric relaxation, and strong interfacial polarization effects, cobalt-substituted copper ferrites ($Co_xCu_{1-x}Fe_2O_4$) are promising candidates for a range of electronic and functional device applications. The observed transition from long-range polaron hopping in Cu-rich samples to localized dielectric relaxation in Co-rich compositions makes these spinels suitable for high-frequency electromagnetic interference (EMI) shielding, magnetoelectric sensors, and high-permittivity dielectric components [60–62]. The increase of onset frequency (ω_H up to 87 kHz), combined with significant AC conductivity and frequency-dependent activation energy, further indicates potential for microwave absorption and impedance-tunable varistors [63]. Moreover, the ability to engineer charge dynamics and carrier localization through controlled cation distribution provides a pathway for optimizing these ferrites in spintronic devices, magnetoresistive elements, and multifunctional memory architectures [64–66]. To further contextualize these findings in terms of state-of-the-art ferrite applications, a benchmarking analysis is provided below.

3.4.5 *Applied relevance*

To contextualize the dielectric and transport behavior of $Co_xCu_{1-x}Fe_2O_4$ ferrites, it is useful to benchmark them against representative ferrite and composite systems (Table 8). Conventional soft ferrites such as NiZn and MnZn typically exhibit onset frequencies (ω_H) below 10 kHz, limiting their performance in high-frequency regimes, despite their widespread use in EMI filters, power electronics, and sensors. By comparison, the present Co-substituted Cu ferrites reach ωH values up to 87 kHz, placing them among the faster-responding spinel systems reported to date. This frequency upshift is particularly advantageous for microwave absorption and EMI shielding, where rapid polarization and relaxation are needed to dissipate incident energy.

Other complex ferrite systems, such as CoMnZn or YbCoZn, show enhanced dielectric constants and interfacial polarization but remain constrained by ωH near the 10 kHz regime. Similarly, ferrite–polymer or ferrite–nanocarbon composites (e.g., PVDF–ZFO–SDS and $CoFe_2O_4$/carbon) improve dielectric constant or conductivity through interfacial engineering, yet their behavior is strongly dependent on filler content and percolation pathways. In contrast, $Co_xCu_{1-x}Fe_2O_4$ achieves comparable improvements through intrinsic cation redistribution and oxygen-vacancy formation, without the need for composite additives.

From a design perspective, the tunable conduction pathway is the distinctive advantage of the present system. Cu-rich ferrites favor long-range Fe^{2+}/Fe^{3+} hopping, resulting in relatively low activation energies and moderate dielectric losses, suitable for capacitors and varistors. In contrast, Co-rich ferrites ($x \geq 0.8$) exhibit localized dielectric relaxation and high ωH, making them particularly suited for high-frequency EMI shielding, microwave absorbers, and impedance-tunable devices. Intermediate compositions ($x = 0.4–0.6$) provide a balance between conduction and relaxation, offering promise for energy-storage capacitors and multifunctional components.

The benchmarking underscores that the $Co_xCu_{1-x}Fe_2O_4$ series bridges the gap between conventional soft ferrites and engineered ferrite composites, providing comparable or superior frequency response through controlled cation distribution. These findings position the system as a versatile and tunable platform for next-generation electronic, spintronic, and electromagnetic devices, with EMI shielding applications identified as a key direction for future experimental validation.

4 Conclusion

In this study, a series of $Co_xCu_{1-x}Fe_2O_4$ ($x = 0.0–1.0$) ferrite samples were synthesized via the citrate sol–gel autocombustion method and systematically investigated over broad temperature and frequency ranges to elucidate their charge transport behavior.

Electrical conductivity increased with temperature for all compositions, consistent with thermally activated processes. In Co-rich samples ($x = 0.8$ and 1.0), a pronounced slope change in the ln(σT) vs. 1000/T plots

Table 8 Benchmarking of dielectric/transport properties of $Co_xCu_{1-x}Fe_2O_4$ ferrites against representative ferrite systems

Material system	Frequency range (ω_H)	Dielectric/conduction behavior	Typical application relevance	Reference
NiZnCo ferrite	10 kHz to 120 MHz	ε′ and tan δ decrease with increasing frequency and Co content; conduction via Fe^{2+}/Fe^{3+} hopping. Impedance decreases with T and frequency.	High-frequency applications, energy storage, and microelectronics	[67]
MnZn ferrite	~ 10 kHz	Higher σ_{DC} than pure Mn ferrite; conduction via electron hopping between localized states (VRH)	Power electronics, EMI filters, magnetic cores, sensors, biomedical	[68]
YbCoZn ferrite	< 10 kHz	High ε′ at low frequencies due to interfacial polarization; decreases with frequency/Yb content. Grain effects dominate conduction	Magnetoelectric applications, EM-enhanced devices	[69]
CoMnZn ferrite	~ 10 kHz	ε′ and ε″ decrease with frequency (Maxwell–Wagner + Koops' theory). High AC resistivity at low frequencies, reduced at high f	High-frequency EM devices requiring low ε′ and loss	[70]
PVDF-ZFO-SDS composites	100 Hz to 1 MHz	ε′ high at low f due to space-charge polarization; ε′ increases with SDS/ZFO content; σAC increasing with f and filler loading (TPT)	Energy storage, high-ε′ dielectrics, ferroelectric devices	[71]
$CoFe_2O_4$/Carbon nanocomposites	0.01 Hz	Low Rct reduced by carbon; nanointerfaces create conductive networks enhancing charge transport	Electrochemical supercapacitors, magnetically assisted devices	[72]
$Co_xCu_{1-x}Fe_2O_4$ (present study)	up to 87 kHz	Transition from long-range Fe^{2+}/Fe^{3+} hopping (Cu-rich) to localized relaxation and Co^{2+}/Co^{3+} valence fluctuations (Co-rich). Tunable via cation redistribution	High-frequency EMI shielding, microwave absorption	This work

above 373 K signaled a transition in the dominant conduction mechanism. At low temperatures (298–348 K), conduction was primarily governed by grain boundary effects and defect-assisted hopping, showing strong frequency dispersion but weak temperature dependence. At elevated temperatures, long-range small-polaron hopping between Fe^{3+}/Fe^{2+} ions at B-sites dominated, while increasing cobalt substitution introduced additional Co^{2+}/Co^{3+} valence fluctuations, producing a more complex transport landscape.

XPS analysis confirmed that Fe is predominantly Fe^{3+} with minor Fe^{2+}, Cu is mainly Cu^{2+} with traces of Cu^{0}/Cu^{+}, and Co exists largely as Co^{2+} with partial oxidation to Co^{3+} in Co-rich ferrites. The coexistence of Fe^{3+}/Fe^{2+} and Co^{2+}/Co^{3+} redox couples, combined with an increased concentration of oxygen-vacancy–related states, establishes multiple charge-transfer channels. This spectroscopic evidence directly links cation redistribution and defect chemistry to the observed transition from long-range polaron hopping in Cu-rich samples to localized dielectric relaxation and interfacial polarization in Co-rich compositions.

Dielectric analysis further supported this conclusion. The frequency-dependent decrease in activation energy indicated enhanced carrier mobility under alternating fields. Modeling with Jonscher's power law, its modified form, and the Almond–West model captured both long-range and localized conduction processes. Notably, anomalously high dispersion parameters ($s > 1$, $m > 1$) in Co-rich compositions highlighted the dominance of short-range dipolar relaxation and interfacial polarization. The Almond–West analysis revealed a composition-driven increase in onset frequency ω_H from ~ 4 kHz ($CuFe_2O_4$) to ~ 87 kHz ($CoFe_2O_4$), providing a quantitative marker of accelerated carrier dynamics in Co-substituted ferrites.

These findings, reinforced by Koops' model, establish that cation redistribution, valence fluctuations, and oxygen-vacancy formation govern the dielectric and transport behavior of $Co_xCu_{1-x}Fe_2O_4$. The compositional tunability demonstrated here highlights the potential of these ferrites for high-frequency applications such as EMI shielding, capacitive components, and impedance-based sensors.

Acknowledgements

J. Mazurenko acknowledge the Polish National Agency for Academic Exchange. Authors thank the Ministry of Education and Science of Ukraine for funding the project 24BF051-01M (0124U001654). J. Mazurenko acknowledges the National Scholarship Programme of the Slovak Republic for the Support of Mobility of Students, PhD Students, University Teachers, Researchers and Artists for financial support (application number 53157). The authors gratefully acknowledge the support and inspiration provided by the II European Chemistry School for Ukrainians (https://acmin.agh.edu.pl/en/detail/s/ii-european-chemistry-school-for-ukrainians), which contributed to the development of the research ideas presented in this work.

Author contributions

Mazurenko J: Conceptualization; Investigation; Writing—review & editing; Funding acquisition. Kaykan L: Conceptualization; Methodology; Validation; Writing—Original Draft; Moklyak V: Validation; Investigation; Resources; Marzec M: Investigation; Data curation; Formal analysis; Matzui L: Formal analysis; Data curation; Supervision; Vovchenko L: Formal analysis; Data curation; Supervision; Yakovenko O: Formal analysis; Funding acquisition.

Funding

Open access funding provided by The Ministry of Education, Science, Research and Sport of the Slovak Republic in cooperation with Centre for Scientific and Technical Information of the Slovak Republic. This work was funded by Narodowa Agencja Wymiany Akademickiej,BPN/ULM/2022/1/00093,Julia Mazurenko,Ministry of Education and Science of Ukraine,24BF051-01 M (0124U001654),Olena Yakovenko,24BF051-01 M (0124U001654),Julia Mazurenko,Slovak Academic Information Agency,53157,Julia Mazurenko

Data availability

Data is contained within the article.

Declarations

Conflict of interest The authors declare no conflict of interest.

References

1. S. Thammarong, X. Yu, P. Yin, R. Yang, W. Zhang, Co2+ doped zinc manganese ferrite nanoparticles for magnetic induction hyperthermia. J. Magn. Magn. Mater. **628**, 173216 (2025). https://doi.org/10.1016/j.jmmm.2025.173216
2. J. Duan, S. Fan, X. Li, S. Liu, Enhanced conversion of methane to liquid-phase oxygenates via hollow ferrite nanotube@horseradish peroxidase based photoenzymatic catalysis. Appl. Catal. B Environ. Energy **361**, 124593 (2025). https://doi.org/10.1016/j.apcatb.2024.124593
3. A.A. Ibrahim, M. Saed, S.A. Abdullah, K. Dellinger, S.O. Obare, G. Pathiraja, Magnetic zinc ferrite nanostructures: recent advancements for environmental and biomedical applications. J. Alloys Compd. Commun. **4**, 100038 (2024). https://doi.org/10.1016/j.jacomc.2024.100038
4. K. Paulovicova, M. Rajnak, J. Tothova, B. Dolnik, M. Timko, P. Kopcansky, Rheodielectric study of transformer-oil-based ferrofluids. Phys. Rev. E (2025). https://doi.org/10.1103/physreve.111.045403
5. B. Patil, V.M. Jali, Z. Li, N. Shukla, S.F. Shaikh, M. Ubaidullah, B. Chethan, V. Jagadeesha Angadi, Tailoring structural, magnetic, and humidity sensing properties of Cu-Zn ferrites for multifunctional sensor applications. Ceram. Int. (2025). https://doi.org/10.1016/j.ceramint.2025.05.020
6. O. Yakovenko, L. Matzui, L. Vovchenko, V. Zagorodnii, Experimental studies of absorption properties of polymer composites based on core–shell fillers with hybrid shells. Ceram. Int. **50**(24), 52480–52489 (2024). https://doi.org/10.1016/j.ceramint.2024.10.099
7. V. Seetha Rama Raju, C-TAB and magnetic field assisted hydrothermal synthesis of cobalt ferrite for the mid-range 5G frequency band applications. J. Magn. Magn. Mater. **628**, 173146 (2025). https://doi.org/10.1016/j.jmmm.2025.173146
8. B.K. Ostafiychuk, L.S. Kaykan, J.S. Mazurenko, B.Y. Deputat, S.V. Koren, Effect of substitution on the mechanism of conductivity of ultra dispersed lithium - iron spinel, substituted with magnesium ions. J. Nano-Electron. Phys. **9**(5), 05018-1-05018–6 (2017). https://doi.org/10.21272/jnep.9(5).05018
9. B. Naresh, N. Hari Kumar, J.L. Naik, The effects of Ce3+ ions on the structural, optical, Raman, photoluminescence, photocatalysis, magnetic, and electric properties of Co-Mg-Bi ferrites. Ceram. Int. **51**(20), 32033–32048 (2025). https://doi.org/10.1016/j.ceramint.2025.04.393
10. LYu. Matzui, O.A. Syvolozhskyi, L.L. Vovchenko, O.S. Yakovenko, T.A. Len, O.V. Ischenko, A.V. Vakaliuk, V.V. Oliynyk, V.V. Zagorodnii, A. Naumenko, M. Cojocari, G. Fedorov, P. Kuzhir, Segregated conductive polymer composite with Fe3O4-decorated graphite nanoparticles for microwave shielding. Materials **17**(12), 2808 (2024). https://doi.org/10.3390/ma17122808
11. D. Wen, J. Zhang, A. Kulikov, J. Cui, Z. Chen, Z. Wang, Q. Zhang, J. Guo, R. Li, The effect of Al3+ ion substitution on microwave dielectric and magnetic properties of YIG ferrites. Ceram. Int. **51**(5), 6272–6280 (2025). https://doi.org/10.1016/j.ceramint.2024.12.072
12. S. Nayak, S.S. Nayak, A.A. Kittur, S. Nayak, D.R. Joshi, Synthesis, fabrication, and performance evaluation of lanthanum doped nickel cobalt ferrite electrode for supercapacitors in energy storage applications. J. Energy Storage **101**, 113918 (2024). https://doi.org/10.1016/j.est.2024.113918
13. Z. Wang, S. Lei, C. Liu, L. Zhang, X. Ma, M. Gao, Q. Li, C. Chen, W. Zhao, Facile synthesis and green high-performance electromagnetic wave absorbing composite material based on biomass cotton and Ni @ nanoporous carbon. Chem. Phys. **595**, 112716 (2025). https://doi.org/10.1016/j.chemphys.2025.112716
14. N.Y. Ivanichok, I.M. Budzuliak, M.I. Moiseienko, R.P. Lisovskiy, B.I. Rachii, A.M. Gamarnyk, L.V. Turovska, S.A. Lisovska, Electrochemical properties of nanoporous carbon materials obtained from raw materials of plant origin

(hemp shives). Фізика і хімія твердого тіла **21**(1), 35–42 (2020). https://doi.org/10.15330/pcss.21.1.35-42

15. X. Wu, A. Dong, S. Xu, H. Huang, K. Xiao, Y. Jiang, K. Wang, X. Zhang, Efficient broadband sea urchin-like Fe3O4@C electromagnetic wave absorbing materials. J. Magn. Magn. Mater. **600**, 172124 (2024). https://doi.org/10.1016/j.jmmm.2024.172124
16. D. Fei, Y. Guo, J. Zhou, J. Tao, N. Chen, Z. Yao, X. Tao, L. Duan, J. Liu, B. Ouyang, Chemical silver plating synergistically enhances the contribution of interfaces and defects in the Ni-Zn-Nd spinel ferrite-based electromagnetic wave absorbing material. Mater. Res. Bull. **173**, 112662 (2024). https://doi.org/10.1016/j.materresbull.2023.112662
17. Q.J. Ziadzi, H. Wu, K. Deng, Y. Li, B. Chao, S. Deng, F. Zhang, Development of lightweight microwave-absorbing composites incorporating NFG/MZFO resin-matrix materials via selective laser sintering. J. Mater. Res. Technol. (2025). https://doi.org/10.1016/j.jmrt.2025.06.005
18. Y. Duan, Z. Xie, M. Du, X. Feng, Q. Chang, Microwave-assisted rapid synthesis of NiCo2O4 with high-performance electromagnetic wave absorption. J. Magn. Magn. Mater. **629**, 173207 (2025). https://doi.org/10.1016/j.jmmm.2025.173207
19. P. Kumar, P. Negi, A.K. Dixit, H.B. Baskey, S. Kumar, A.K. Mishra, A. Kumar, Superparamagnetic nanocubes of Co and Cu co-doped Mn-based ferrites as microwave absorbing material. Mater. Chem. Phys. **319**, 129360 (2024). https://doi.org/10.1016/j.matchemphys.2024.129360
20. S.H. Dewi, D.S. Winatapura, J. Setiawan, A. Mulyawan, Y.E. Gunanto, W.A. Adi, Exploring the structural and magnetic properties of La-doped nickel ferrite for microwave absorbing application. J. Magnet. Magnet. Mater. **603**, 172267 (2024). https://doi.org/10.1016/j.jmmm.2024.172267
21. Z. Lin, S. Hao, Z. Li, J. Hu, A. Song, Elucidation of the optical, electronic, and photoelectrochemical properties of p-type CuFe2O4 photocathodes. Int. J. Hydrogen Energy **77**, 511–519 (2024). https://doi.org/10.1016/j.ijhydene.2024.06.248
22. S.N. Khan, A. Mir, I. Saeed, I. Sultana, H.T. Masood, Effect of cobalt substitution on electromagnetic response of Manganese-Zinc spinel ferrite composite. Mater. Sci. Eng. B Solid-State Mater. Adv. Technol. **319**, 118344 (2025). https://doi.org/10.1016/j.mseb.2025.118344
23. I.S. Kapte, S. Niyogi, P.J. Qureshi, V. Khade, T. Avanish Babu, K.V. Siva kumar, W. Madhuri, Microwave assisted cobalt nickel ferrite as exhaust thrust sensor and EMI shield. Ceram. Int. **50**(17), 30754–30762 (2024). https://doi.org/10.1016/j.ceramint.2024.05.376
24. J. Mazurenko, E. Szostak, L. Gondek, L. Kaykan, A. Zywczak, O. Vyshnevskyi, Structural and magnetic studies of Cobalt-substituted copper ferrites for efficient photocatalytic dye degradation. Inorg. Chem. Commun. **171**, 113648 (2025). https://doi.org/10.1016/j.inoche.2024.113648
25. L.S. Kaykan, J.S. Mazurenko, N.V. Ostapovych, A.K. Sijo, N.Y. 'Ivanichok, Effect of pH on structural morphology and magnetic properties of ordered phase of cobalt doped lithium ferrite nanoparticles synthesized by sol-gel autocombustion method. J. Nano-Electron. Phys. **12**(4), 04008-1-04008–7 (2020). https://doi.org/10.21272/jnep.12(4).04008
26. Z. Wang, J. Huang, L. Wang, Y. Liu, W. Liu, S. Zhao, Z. Liu, Cation-tuning induced d-band center modulation on Co-based spinel oxide for oxygen reduction/evolution reaction. Angew. Chem. (2022). https://doi.org/10.1002/ange.202114696
27. L. Song, H. Zhang, J. Xiong, Z. Chen, Y. Liu, H. Zhou, W. Yang, D. Cao, H. Huang, L. Chen, M. Fu, D. Ye, Doped Mn modulates the local charge distribution of cobalt-based spinel catalysts to promote the availability of ligand lattice oxygen for complete oxidation of methane. Appl. Catal. B Environ. **343**, 123547 (2024). https://doi.org/10.1016/j.apcatb.2023.123547
28. A.P. Grosvenor, B.A. Kobe, M.C. Biesinger, N.S. McIntyre, Investigation of multiplet splitting of Fe 2p XPS spectra and bonding in iron compounds. Surf. Interface Anal. **36**(12), 1564–1574 (2004). https://doi.org/10.1002/sia.1984
29. M.C. Biesinger, B.P. Payne, A.P. Grosvenor, L.W.M. Lau, A.R. Gerson, R.S.C. Smart, Resolving surface chemical states in XPS analysis of first row transition metals, oxides and hydroxides: Cr, Mn, Fe, Co and Ni. Appl. Surf. Sci. **257**(7), 2717–2730 (2011). https://doi.org/10.1016/j.apsusc.2010.10.051
30. M.C. Biesinger, Advanced analysis of copper X-ray photoelectron spectra. Surf. Interface Anal. **49**(13), 1325–1334 (2017). https://doi.org/10.1002/sia.6239
31. P.C. Healy, S. Myhra, A.M. Stewart, XPS studies of planar four-coordinate copper(II) and copper(III) complexes. Jpn. J. Appl. Phys. **26**(11), L1884–L1887 (1987). https://doi.org/10.1143/JJAP.26.L1884
32. T.J. Chuang, C.R. Brundle, D.W. Rice, Interpretation of the x-ray photoemission spectra of cobalt oxides and cobalt oxide surfaces. Surf. Sci. **59**(2), 413–429 (1976). https://doi.org/10.1016/0039-6028(76)90026-1
33. N.S. McIntyre, M.G. Cook, X-ray photoelectron studies on some oxides and hydroxides of cobalt, nickel, and copper. Anal. Chem. **47**(13), 2208–2213 (1975). https://doi.org/10.1021/ac60363a034

34. K. Ugendar, G. Markandeyulu, S. Mallesh, Polaron conduction mechanism in Nickel ferrite and its rare-earth derivatives. Phys. B Condens. Matter **606**, 412819 (2021). https://doi.org/10.1016/j.physb.2021.412819
35. A.M. Abdeen, Electric conduction in Ni–Zn ferrites. J. Magn. Magn. Mater. **185**(2), 199–206 (1998). https://doi.org/10.1016/s0304-8853(97)01144-x
36. R.A. Mondal, B.S. Murty, V.R.K. Murthy, Maxwell-Wagner polarization in grain boundary segregated NiCuZn ferrite. Curr. Appl. Phys. **14**(12), 1727–1733 (2014). https://doi.org/10.1016/j.cap.2014.10.005
37. E. Veena Gopalan, K.A. Malini, S. Saravanan, D. Sakthi Kumar, Y. Yoshida, M.R. Anantharaman, Evidence for polaron conduction in nanostructured manganese ferrite. J. Phys. D Appl. Phys. **41**(18), 185005 (2008). https://doi.org/10.1088/0022-3727/41/18/185005
38. P.J. Phillips, T.E. Whall, V.A.M. Brabers, Hopping conduction and possible Coulomb gap effects in manganese and zinc ferrous ferrite. Philos. Mag. B **71**(1), 23–39 (1995). https://doi.org/10.1080/01418639508240290
39. L.S. Kaykan, J.S. Mazurenko, I.P. Yaremiy, K.V. Bandura, N.V. Ostapovych, Effect of nickel ions substitution on the structural and electrical properties of a nanosized lithium-iron ferrite obtained by the sol-gel auto-combustion method. J. Nano- Electron. Phys. **11**(5), 05041-1-05041–05047 (2019). https://doi.org/10.21272/jnep.11(5).05041
40. S.K. Mandal, S. Singh, P. Dey, J.N. Roy, P.R. Mandal, T.K. Nath, Frequency and temperature dependence of dielectric and electrical properties of TFe 2 O 4 (T = Ni, Zn, Zn 0.5 Ni 0.5) ferrite nanocrystals. J. Alloys Compd. **656**, 887–896 (2016). https://doi.org/10.1016/j.jallcom.2015.10.045
41. P. Chand, S. Vaish, P. Kumar, Structural, optical and dielectric properties of transition metal (MFe2O4; M = Co, Ni and Zn) nanoferrites. Phys. B Condens. Matter **524**, 53–63 (2017). https://doi.org/10.1016/j.physb.2017.08.060
42. A.A. Khan, M.U. Fayaz, M.N. Khan, M. Iqbal, A. Majeed, R. Bilkees, S. Mukhtar, M. Javed, Investigation of charge transport mechanism in semiconducting La0.5Ca0.5Mn0.5Fe0.5O3 manganite prepared by sol–gel method. J. Mater. Sci. Mater. Electron. **29**(16), 13577–13587 (2018). https://doi.org/10.1007/s10854-018-9485-2
43. T. Das, J.D. Nicholas, Y. Qi, Long-range charge transfer and oxygen vacancy interactions in strontium ferrite. J. Mater. Chem. A **5**(9), 4493–4506 (2017). https://doi.org/10.1039/c6ta10357j
44. M. Azizar Rahman, A.K.M. Akther Hossain, Electrical transport properties of Mn–Ni–Zn ferrite using complex impedance spectroscopy. Phys. Scr. **89**(2), 025803 (2014). https://doi.org/10.1088/0031-8949/89/02/025803
45. A. Lungu, I. Malaescu, C.N. Marin, P. Vlazan, P. Sfirloaga, The electrical properties of manganese ferrite powders prepared by two different methods. Phys. B Condens. Matter **462**, 80–85 (2015). https://doi.org/10.1016/j.physb.2015.01.025
46. C.G. Koops, On the dispersion of resistivity and dielectric constant of some semiconductors at audiofrequencies. Phys. Rev. **83**(1), 121–124 (1951). https://doi.org/10.1103/physrev.83.121
47. R.K. Panda, D. Behera, Investigation of electric transport behavior of bulk CoFe2O4 by complex impedance spectroscopy. J. Alloys Compd. **587**, 481–486 (2014). https://doi.org/10.1016/j.jallcom.2013.10.195
48. S. Minz, S.C. Sahoo, S.K. Rout, B. Behera, Structural, temperature/frequency dependence of dielectric, electrical and magnetic properties of Ni-doped inverse spinel CuFe2O4 nanoferrite. J. Mater. Sci. Mater. Electron. (2023). https://doi.org/10.1007/s10854-022-09791-5
49. R.K. Panda, R. Muduli, S.K. Kar, D. Behera, Dielectric relaxation and conduction mechanism of cobalt ferrite nanoparticles. J. Alloys Compd. **615**, 899–905 (2014). https://doi.org/10.1016/j.jallcom.2014.07.031
50. R. Tang, C. Jiang, W. Qian, J. Jian, X. Zhang, H. Wang, H. Yang, Dielectric relaxation, resonance and scaling behaviors in Sr3Co2Fe24O41 hexaferrite. Sci. Rep. (2015). https://doi.org/10.1038/srep13645
51. A. Messaoudi, A. Omri, N. Hamdaoui, A. Benali, R. Ajjel, M.F.P. Graca, B.F.O. Costa, K. Khirouni, Advanced spinel ferrite Co06Zn03Ca01Fe2O4 nanoparticles: structural, optical, and electrical insights for functional applications. J. Australian Ceram. Soc. (2025). https://doi.org/10.1007/s41779-025-01235-7
52. R.S.A. Raj, A. Joseph, S. Hussain, M. Fahad, T. Maity, P.M. Sarun, L.K. Joy, Frequency and temperature dependent dielectric properties of CoFe2−xYxO4: polarization and conduction mechanisms related to crystallographic symmetry and electronic transitions. J. Mater. Chem. C **13**(11), 5880–5910 (2025). https://doi.org/10.1039/d4tc04677c
53. M. Murtaza, M.U. Islam, M. Danish, M. Waqas, F. Ahmad, S. Atiq, M. Alsharef, A. Althobaiti, Synthesis and multifunctional properties of Ni-Co Co-doped lithium ferrites for structural, electrical, and dielectric performance in device applications. Ionics **31**(6), 6495–6512 (2025). https://doi.org/10.1007/s11581-025-06342-w
54. R. Megha, Y.T. Ravikiran, S.C. Vijaya Kumari, S. Thomas, Influence of n-type nickel ferrite in enhancing the AC conductivity of optimized polyaniline-nickel ferrite nanocomposite. Appl. Phys. A (2017). https://doi.org/10.1007/s00339-017-0866-9

55. R.N. Bhowmik, Temperature- and frequency-activated semiconductor-to-metal transition in soft ferromagnetic Li0.5Mn0.5Fe2O4ferrite. Mater. Res. Express **1**(1), 015903 (2014). https://doi.org/10.1088/2053-1591/1/1/015903
56. Y. Abbas, M. Anis-ur-Rehman, Structural, dielectric and transport properties of samarium-doped cobaltites. Ceram. Int. **48**(8), 10638–10649 (2022). https://doi.org/10.1016/j.ceramint.2021.12.278
57. S. Lenka, T. Badapanda, P. Nayak, S. Sarangi, S. Anwar, Compositional induced dielectric relaxation and electrical conduction behavior of samarium modified bismuth sodium titanate ceramic. Ceram. Int. **47**(4), 5477–5486 (2021). https://doi.org/10.1016/j.ceramint.2020.10.130
58. S. Minz, S.C. Sahoo, S.K. Rout, M. Kar, B. Behera, Structural, magnetic, impedance and electric modulus response and dielectric relaxation in Co-doped inverse spinel CuFe2O4 nanoferrite. Chem. Phys. Impact **8**, 100592 (2024). https://doi.org/10.1016/j.chphi.2024.100592
59. D.P. Almond, A.R. West, Anomalous conductivity prefactors in fast ion conductors. Nature **306**(5942), 456–457 (1983). https://doi.org/10.1038/306456a0
60. O. Yakovenko, L. Matzui, L. Vovchenko, Y. Perets, D. Shpylka, L. Kaykan, A. Żywczak, Ł Gondek, J. Mazurenko, Electrodynamic properties of epoxy composites enhanced with nanosized ferrite fillers. Ceram. Int. (2025). https://doi.org/10.1016/j.ceramint.2025.05.151
61. B. Chandra Sekhar, G.S.N. Rao, O.F. Caltun, B. Dhana Lakshmi, B. Parvatheeswara Rao, P.S.V. Subba Rao, Magnetic and magnetostrictive properties of Cu substituted Co-ferrites. J. Magn. Magn. Mater. **398**, 59–63 (2016). https://doi.org/10.1016/j.jmmm.2015.09.028
62. A. Murugan, V. Siva, A. Shameem, R. Deepika, S. Bharathkumar, H. Valdés, S.A. Bahadur, Electrochemical properties of nanoscale Cu Co spinel ferrite system: a promising positive electrode for high performance supercapacitors. J. Energy Storage **99**, 113179 (2024). https://doi.org/10.1016/j.est.2024.113179
63. M. Hjiri, S. Soltani, A. Jbeli, N. Mustapha, N. Ahmed Althumairi, M. Benamara, M.A. Valente, Tunable electrical properties of cobalt-doped maghemite nanoparticles for advanced resistive and thermistor applications. Nanomaterials **15**(7), 534 (2025). https://doi.org/10.3390/nano15070534
64. A. Hirohata, H. Sukegawa, H. Yanagihara, I. Zutic, T. Seki, S. Mizukami, R. Swaminathan, Roadmap for emerging materials for spintronic device applications. IEEE Trans. Magn. **51**(10), 1–11 (2015). https://doi.org/10.1109/tmag.2015.2457393
65. K.V. Siva, A. Kumar, J.A. Chelvane, A. Arockiarajan, Structural, magnetic, magnetostrictive and optical properties of Mn and Cu codoped cobalt ferrite. Mater. Sci. Eng. B Solid-State Mater. Adv. Technol. **284**, 115885 (2022). https://doi.org/10.1016/j.mseb.2022.115885
66. K.V. Ramesh, D. Venkatesh, Effect of copper substitution on structural, electrical, and magnetic properties of nanocrystalline cobalt ferrites for memory storage applications. Physica Status Solidi (b) (2024). https://doi.org/10.1002/pssb.202400453
67. S. Jangra, P. Thakur, S. Singh, A. Thakur, Frequency and temperature dependent impedance studies: impact of cobalt substitution on Ni-Zn ferrites for high frequency applications. Inorg. Chem. Commun. **174**, 113948 (2025). https://doi.org/10.1016/j.inoche.2025.113948
68. I. Malaescu, P. Sfirloaga, C.N. Marin, M.O. Bunoiu, P. Vlazan, Experimental investigations on the electrical conductivity and complex dielectric permittivity of ZnxMn1−xFe2O4 (x = 0 and 0.4) ferrites in a low-frequency field. Crystals **14**(5), 437 (2024). https://doi.org/10.3390/cryst14050437
69. H. Badiger, B.G. Hegde, S.P. Kubrin, N. Chougala, S. Matteppanavar, Structural, magnetic, electrical, and Mössbauer study of Yb-doped cobalt zinc ferrite nanoparticles. J. Mater. Sci. Mater. Electron. (2025). https://doi.org/10.1007/s10854-025-15632-y
70. P. Saha, S.K. Shil, P. Roy, R.S. Auntu, N.I. Khan, S.S. Sikder, Exploring the structural, magnetic, dielectric and electrical properties of solid state method synthesized Mn3+ substituted Co–Zn ferrites. J. Mater. Sci. **60**(37), 17051–17064 (2025). https://doi.org/10.1007/s10853-025-11449-6
71. M. Sethy, S. Moharana, S. Chakroborty, S.C. Sahu, B. Behera, R.N. Mahaling, N. Asthana, Effect of sodium dodecyl sulfate on the dielectric and electrical properties of poly (vinylidene fluoride)-zinc ferrite composites. J. Mol. Struct. **1321**, 139782 (2025). https://doi.org/10.1016/j.molstruc.2024.139782
72. K. Prabakaran, T. Kavinkumar, M. Shafi, L.R. Shobin, R.V. Mangalaraja, V.R. Bhaviripudi, C.V. Abarzúa, A. Thirumurugan, Pyrolytic carbon decorated cobalt ferrite nanostructures as a negative electrode material for improved supercapacitor applications. Diamond Relat. Mater. **151**, 111822 (2025). https://doi.org/10.1016/j.diamond.2024.111822